nature communications

Article

https://doi.org/10.1038/s41467-026-72471-z

Interfacial anionic competition-driven electrochemical evolution in FeF_3 conversion electrodes

Received: 8 April 2025

Accepted: 7 April 2026

Published online: 05 May 2026

Check for updates

Ziang Jiang[1,7,8], Shunrui Luo[2,3,8], Pengfei Wang[1], Jiali Peng[4], Ming Hao[1], Fulu Chu[1], Jie Lei[5], Paulo Ferreira[3,6] & Feixiang Wu[1]

Iron trifluoride demonstrates poor performance as a multi-electron conversion positive electrode in conventional ester-based electrolytes, yet exhibits higher capacity retention in ether-based electrolytes. This contrast has long remained unresolved in high-energy-density metal fluoride-lithium batteries. Here, we show that the electrolyte-dependent behavior originates from interfacial anion competition within the cathode-electrolyte interphase. Spectroscopic and electrochemical analyses reveal that anions derived from lithium salts preferentially interact with iron species, governing interfacial conversion pathways and phase evolution. In ether-based electrolytes, lithium sulfide and lithium oxide react with iron to form electrochemically active iron sulfide species, sustaining reversible cycling. In contrast, lithium carbonate formed in ester-based electrolytes leads to inert carbonate-rich iron species, resulting in surface passivation and capacity decay. With prolonged cycling, iron trifluoride gradually evolves into thermodynamically stable iron-based phases, highlighting that interfacial anion chemistry dictates long-term phase evolution and degradation pathways of iron-based fluoride conversion electrodes.

Lithium batteries are among the most widely used power sources for electric vehicles, offering an eco-friendly and energy-efficient alternative to conventional fuel cars[1]. To achieve long-range electric vehicles and even electric airliners, increasing the energy density of power batteries is crucial[2]. However, the energy density of traditional intercalation-type positive electrodes in lithium batteries has reached a bottleneck, while the associated costs remain high[3]. Among various next-generation candidates, iron trifluoride (FeF_3) has drawn significant attention as a conversion-type positive electrode that operates within 1.0–4.0 V and delivers a high theoretical specific capacity of 712 mAh g^{-1} at an average voltage of 2.74 V versus Li^+/Li[4–6]. The FeF_3 positive electrode also offers advantages of low cost, high abundance, and environmental compatibility, making it a promising candidate for large-scale energy storage applications. Nevertheless, FeF_3 suffers from severe voltage hysteresis, sluggish reaction kinetics, and poor reversibility, which hinder its practical deployment. Extensive optimization efforts have been made in both material engineering and electrolyte formulation, yielding notable progress[7–10].

Carbon composite architectures, nanoscale engineering, and heteroatom doping strategies have improved the reaction kinetics and electronic conductivity of FeF_3-based positive electrodes[11–13]. However, it has become increasingly evident that the electrolyte exerts an even

[1]School of Metallurgy and Environment, Central South University, Changsha, PR China. [2]Catalan Institute of Nanoscience and Nanotechnology (ICN2), CSIC and BIST, Campus UAB, Bellaterra, Barcelona, Catalonia, Spain. [3]International Iberian Nanotechnology Laboratory (INL), Braga, Portugal. [4]Institute for Applied Materials (IAM), Karlsruhe Institute of Technology (KIT), Eggenstein-Leopoldshafen, Germany. [5]Institute for New Energy Materials and Engineering, College of Materials Science and Engineering, Fuzhou University, Fuzhou, PR China. [6]Mechanical Engineering Department and IDMEC, Instituto Superior Técnico, University of Lisbon, Lisboa, Portugal. [7]Present address: Department of Chemistry, Oregon State University, Corvallis, OR, USA. [8]These authors contributed equally: Ziang Jiang, Shunrui Luo. e-mail: feixiang.wu@csu.edu.cn

stronger influence on the electrochemical performance of iron fluorides[7,14,15]. In particular, lithium bis(fluorosulfonyl)imide(LiFSI)-based electrolytes (especially ether-based and ionic-liquid systems) have been reported to support reversible electrochemical activity of iron fluoride positive electrodes over extended cycle numbers[16–18]. Conversely, iron fluoride positive electrodes cycled in ester-based systems experience rapid capacity fading and voltage decay, even with optimized electrolyte formulations[14,15,19]. This discrepancy has been widely attributed to differences in the cathode-electrolyte interphase (CEI), which governs interfacial ion transport, structural protection, and side reactions[15,17].

Despite these insights, the underlying reason for the contrasting cycling behaviors in ether- and ester-based systems remains unresolved. Earlier reports have shown that iron-based fluorides exhibit significant evolution in their charge–discharge profiles upon cycling in both types of electrolytes[12,17,19–21], suggesting fundamental differences in their long-term electrochemical pathways. However, most prior studies have focused mainly on the initial conversion reaction ($FeF_3 + 3e^- + 3Li^+ \rightleftharpoons Fe + 3LiF$) while largely neglecting the structural and interfacial transformations that occur during extended cycling[18,22–27]. This oversight risks underestimating the true complexity of FeF_3 positive electrodes, whose reaction chemistry may evolve far beyond the simple Fe–F redox process. Consequently, a critical question arises: after long-term cycling, does FeF_3 still behave as a fluoride-based conversion electrode, or does it transform into a fundamentally different material?

To address this question, we investigated the origin of the performance divergence between ether- and ester-based systems using a nano-engineered FeF_3@ reduced graphene oxide (rGO) composite synthesized via a gas-solid fluorination route. The electrochemical behavior of FeF_3@rGO was systematically evaluated in two representative electrolytes: a highly concentrated electrolyte composed of LiFSI in 1,2-dimethoxyethane (DME) (4.6 M, denoted as LFDM) and a conventional carbonate electrolyte of lithium hexafluorophosphate ($LiPF_6$) in ethylene carbonate (EC)/dimethyl carbonate (DMC) (1:1, v/v, denoted as LPED). Combining electrochemical measurements with multiscale spectroscopic and microscopic characterizations, we investigate the structural and chemical evolution of FeF_3 during extended cycling. Our findings reveal that the phase evolution of FeF_3 is governed by interfacial anion competition, where distinct CEI compositions lead to divergent reaction pathways. In the LFDM electrolyte, Li_2S and Li_2O species enriched in the CEI react with Fe to form electrochemically active sulfide compounds, thereby sustaining reversible cycling. In contrast, in the LPED electrolyte, Li_2CO_3 dominates the CEI, promoting the development of carbonate-rich environments involving $FeCO_3$ coordination, which cause severe capacity decay.

This interfacial anion-competition mechanism establishes a unifying explanation for the electrolyte-dependent behavior of FeF_3 and highlights the catalytic role of nanoscale Fe particles in CEI evolution. The distinct reaction pathways identified here are reminiscent of geochemical transformations of iron minerals under different chemical environments, providing a compelling analogy between electrochemical and natural processes. Our study helps clarify the contrasting behavior of FeF_3 in ether- and ester-based electrolytes and provides mechanistic insight into interfacial redox processes, associated degradation pathways, and phase reconstruction in iron-based fluoride electrodes.

Results

Electrolyte-dependent electrochemical divergence of FeF_3 electrodes

To compare the electrochemical behavior of the FeF_3 positive electrode in the LFDM and LPED electrolytes, we conducted charge-discharge tests using FeF_3@rGO positive electrodes in Li-metal cells. The synthesis and the composite properties of FeF_3@rGO are investigated in Supplementary Figs. 1 and 2. The voltage range of 1.0 to 4.0 V was chosen to enable a three-electron conversion reaction in the FeF_3 positive electrode. As shown in Fig. 1a, the FeF_3@rGO–Li cell in the LFDM electrolyte exhibits an initial discharge capacity of 476.5 mAh g^{-1}, and after 125 cycles (at 0.5 C, where 1 C = 712 mA g^{-1} based on the theoretical capacity of FeF_3, details shown in Supplementary Note 2), it still retains 425.0 mAh g^{-1}, corresponding to a capacity retention of 89.2%, relative to the first discharge capacity. In contrast, the capacity decay in the LPED electrolyte is quite significant, with capacity retention dropping to only 17.3% (from 422.7 mAh g^{-1} to 72.9 mAh g^{-1}). This behavior aligns with previous studies, highlighting the poor reversibility of iron fluoride positive electrodes in ester-based electrolytes. Additional data from parallel cells are provided in Supplementary Fig. 3a to further demonstrate the reproducibility of the electrochemical performance. The rate capability of the electrodes was further evaluated (Supplementary Fig. 3b), showing better performance in the LFDM electrolyte compared with LPED. An interesting phenomenon is observed in LFDM: the specific capacity declines from the 1st to the 50th cycle (to ~407 mAh g^{-1}), but then increases steadily to 425 mAh g^{-1} by the 125th cycle, indicating a phenomenon of capacity increase during prolonged cycling, often referred to as "negative fading," which has also been observed in various conversion-type electrodes[28].

Further observation of the charge-discharge curves at 0.1 C shows that the initial charge-discharge curves of the batteries in two electrolytes are almost identical (Fig. 1b). The differential capacity curves (Fig. 1c) also nearly overlap with reduction reaction voltages of approximately 3.3 V and 2.0 V and oxidation reaction voltages of 3.4 V and 2.9 V. These correspond to the Fe^{3+}/Fe^{2+} and Fe^{2+}/Fe^0 conversions, respectively, which are consistent with previously reported behavior of the FeF_3 positive electrode[8,11,17]. This demonstrates that the initial conversion mechanism of FeF_3 is the same in both electrolytes, and the electrolyte effect becomes evident only upon extended cycling.

However, during 125 cycles at 0.5 C, significant differences emerge in the charge-discharge curves of cells in two electrolytes. Figure 1d displays charge-discharge curves of the cell using the LFDM electrolyte at different cycle numbers where the voltage plateaus gradually decline over cycling, though the overall capacity shows no substantial decay. To track the changes more closely, differential capacity curves from the 1st to 125th cycles at 0.5 C are selected, and the in situ differential capacity plots (the discharge and charge parts) are created, as shown in Fig. 1e, f. A dynamic shift in the redox peaks is clearly observed, with the initial charge-discharge process matching the redox potentials of the first cycle. However, as the reaction progresses, the intensity of the original redox peaks gradually weakens until they completely disappear (around the 125th cycle). Meanwhile, additional redox peaks progressively emerge, with three reduction peaks at 1.4 V, 2.0 V, and 2.7 V, and three oxidation peaks at 1.9 V, 2.4 V, and 3.5 V. These changes suggest that the electrochemical reaction pathway of FeF_3 evolves with cycling, enabling sustained redox activity in LFDM. Under lower-rate conditions (0.2 C, Supplementary Fig. 3c–g), similar negative fading behavior and redox-peak evolution are observed. Commercial FeF_3 (Supplementary Fig. 4) and FeF_2 (Supplementary Fig. 5) electrodes in LFDM also display consistent trends, further supporting the universality of this behavior. Importantly, the same evolving redox behavior and sustained reversible cycling are also observed under lean-electrolyte conditions, indicating that this behavior is not an artifact of excess electrolyte (Supplementary Fig. 6).

In contrast, when using the LPED electrolyte, the shape of the charge-discharge curves also shows significant changes over time, as shown in Fig. 1g. The specific capacity shows a clear trend of decline, accompanied by a rising voltage plateau during charging and a decreasing voltage plateau during discharging. The differential capacity curves reveal that the voltages of discharge redox peaks gradually

https://doi.org/10.1038/s41467-026-72471-z

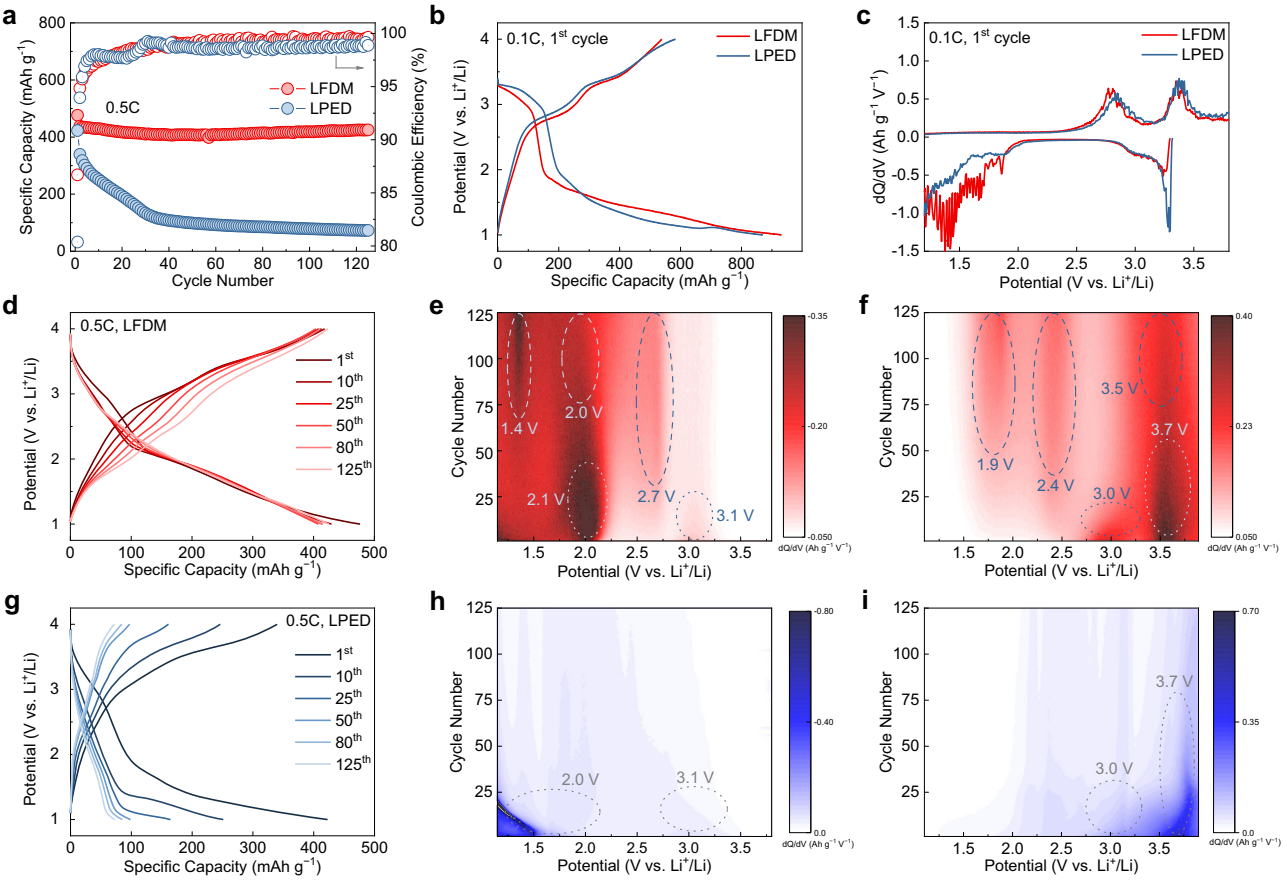

Fig. 1 | Electrochemical performance of FeF_3 electrodes in LFDM and LPED electrolytes. a Comparison of cycling performance at 0.5 C (1 C = 712 mAh g^{-1}). **b** First-cycle charge/discharge profiles at 0.1 C. **c** Differential capacity (dQ/dV) plot during the 1st cycle. **d** Evolution of charge/discharge profiles at 0.5 C in LFDM electrolyte; In situ dQ/dV plots in LFDM electrolyte for the discharge (**e**) and charge (**f**) processes at 0.5 C and 25 ± 1 °C. **g** Evolution of the charge/discharge profiles at 0.5 C in LPED electrolyte. In situ dQ/dV plots in LPED electrolyte for the discharge (**h**) and charge (**i**) processes at 0.5 C and 25 ± 1 °C.

decrease (Fig. 1h), while the voltages of charge redox peaks gradually increase (Fig. 1i), reflecting a progressive loss of electrochemical activity that ultimately leads to cell failure. rGO-only electrodes (Supplementary Fig. 7) confirm negligible intrinsic capacity contribution. Electrochemical Impedance Spectroscopy (EIS), Distribution of Relaxation Times (DRT) (Supplementary Fig. 8), and Cyclic Voltammetry (CV) (Supplementary Fig. 9) analyses show consistent trends with the capacity results, corroborating interfacial stabilization in LFDM versus degradation in LPED[29].

Taken together, these electrochemical results establish a clear contrast: while both electrolytes enable the same initial FeF_3 conversion mechanism, the long-term fate of the positive electrode diverges drastically. LFDM sustains reversible activity with gradually evolving redox features, whereas LPED leads to rapid fading and eventual passivation. Such a sharp divergence implies that the underlying phase evolution of the electrodes must differ significantly. To probe this directly, we performed in situ X-ray diffraction (XRD) measurements (Supplementary Fig. 10); however, no diffraction peaks were observed after extended cycling, consistent with the amorphization of FeF_3 reported in prior studies[21]. This outcome highlights the limitation of conventional diffraction methods in capturing the key transformations.

Interfacial reconstruction reveals distinct anion migration pathways

To observe the morphological evolution of the positive electrode material, scanning electron microscopy (SEM) was performed on pristine electrodes and those cycled for 200 cycles in the two electrolytes (Supplementary Fig. 11). The overall framework of FeF_3@rGO remains intact, with FeF_3 particles uniformly embedded in the graphene layers. However, the average particle size increased from ~86.8 nm (pristine) to 151.7 nm in LFDM and 122.3 nm in LPED, corresponding to growth of 74.8% and 40.9%, respectively. This coarsening is attributed to particle pulverization during conversion reactions and the persistent formation of CEI. High-angle annular dark-field scanning transmission electron microscopy (HAADF–STEM) further shows that in LFDM, particles retain well-defined morphologies after the 1st cycle (Supplementary Fig. 12a, b), but evolve into porous structures by the 10th cycle (Supplementary Fig. 11c), which persist even after 250 cycles (Supplementary Fig. 12d–f). In contrast, in LPED, the porous morphology already appears after the 1st cycle and remains up to 500 cycles (Supplementary Fig. 13). To further examine the crystallinity change, high-resolution transmission electron microscopy (HRTEM) was carried out on cycled samples (Supplementary Fig. 14). The pristine material displays clear lattice fringes with sharp fast Fourier transform (FFT) spots, confirming its crystalline nature. After the 1st cycle, lattice fringes become blurred and the FFT pattern transforms into rings, indicative of nanocrystallite formation. By the 10th cycle, the FFT evolves into a diffuse halo, confirming an amorphous state. This progressive loss of crystallinity upon cycling is consistent with previous reports on transition-metal conversion electrodes[18].

To probe the spatial evolution of FeF_3 within individual particles, transmission electron microscopy (TEM) coupled with electron energy loss spectroscopy (EELS) was employed to analyze FeF_3 positive electrodes at the 1st and 125th cycle in LFDM and LPED electrolytes, as illustrated in Fig. 2. The cycled FeF_3 particles present a pomegranate-like morphology composed of numerous nanosized sub-particles

https://doi.org/10.1038/s41467-026-72471-z

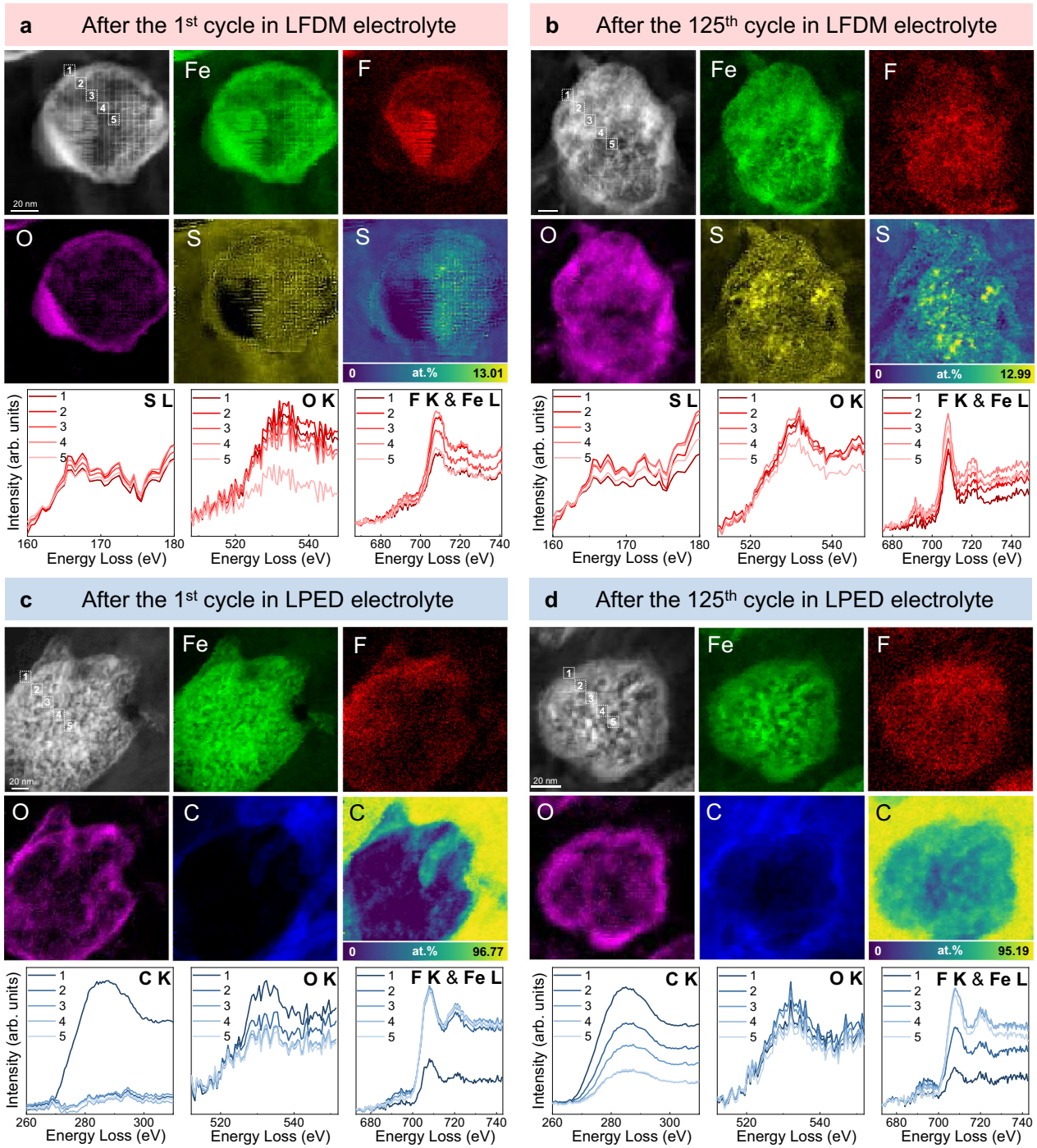

Fig. 2 | Compositional evolution of FeF_3 particles during cycling. HAADF-STEM images and corresponding EELS elemental mappings of FeF_3 particles cycled in LFDM (**a**, **b**) and LPED (**c**, **d**) electrolytes after the first cycle (**a**, **c**) and the 125th cycle (**b**, **d**). Corresponding EELS spectra of the O K-, Fe $L_{2,3}$-, F K-, and S $L_{2,3}$- or C K- edges from five selected subregions indicated in the HAADF images. Cells were cycled between 1.0 and 4.0 V at 0.5 C (1 C = 712 mAh g^{-1}) and 25 ± 1 °C before disassembly.

loosely packed within the original particle framework, compared to the pristine material (Supplementary Fig. 2). This structure reflects repeated breaking and reconstruction of FeF_3 during lithiation and delithiation, accompanied by a gradual loss of long-range order. EELS mapping reveals strong overlap between Fe and F signals, though much lower F signal intensity compared to Fe due to partial decomposition of iron fluorides under electron beam irradiation. After quantification, Fe and F remain broadly co-localized, but additional heterogeneity develops as cycling proceeds.

Notably, the O signals show distinct spatial evolution during cycling. After the 1st charge, oxygen is primarily concentrated at the particle interfaces, likely existing as CEI-related components such as lithium salts. However, after 125 cycles, the O signal intensifies and diffuses into the interior of the FeF_3 particles, exhibiting partial overlap with the Fe signal. This inward diffusion indicates that oxygen-containing species gradually penetrate from the interface into the bulk, forming mixed Fe–O environments, though the exact bonding states cannot be confirmed solely by mapping. The S signal is also

detected in the middle of the FeF_3 particle cycled in the LFDM electrolyte, and the atomic concentration of sulfur clearly increases from the 1st to the 125th cycle. The growing overlap between S and Fe signals suggests stronger Fe–S associations within the bulk. In contrast, in the LPED electrolyte, an increased atomic concentration of carbon is observed after the 125th cycle, together with oxygen enrichment near the particle interior, indicating the progressive incorporation of C/O-containing species. The propagation of the C signal from the edge to the center further supports the inward diffusion of electrolyte-derived components.

Further, sulfur diffusion characteristics were investigated by EELS atomic concentration mapping (Fig. 2a, b). Higher S concentrations were detected in the center than at the edge of the particle after extended cycling. The core-loss components of EELS datasets, corresponding to five subregions of interest (white boxes in the HAADF image), were analyzed from the surface to the center of the FeF_3 particle[30]. The S $L_{2,3}$-edge after 125 cycles shows a gradually increasing intensity from the surface to the center, revealing a compositional gradient of S-containing species, including S– and S = O components. In comparison, the O K-edge exhibits a similar diffusion trend but does not penetrate as deeply as the S species. This difference may originate from the higher mobility and solubility of sulfur-based intermediates (e.g., polysulfides) in the electrolyte, which facilitates their diffusion within the particle during cycling. Meanwhile, the Fe $L_{2,3}$- and F K-signals are distributed randomly and inhomogeneously inside FeF_3 particles, likely due to local migration and redistribution of Fe during repeated conversion reactions[31–33]. Furthermore, elemental mapping analysis based on energy-dispersive X-ray spectroscopy (EDX) (Supplementary Fig. 15) was conducted on the positive electrode sample after 50 cycles to further verify the spatial redistribution of elements. The results clearly reveal the outward migration of Fe ions and the inward diffusion of S and O species from the interface into the bulk. The reduced spatial overlap between Fe and F signals, along with increased correlation between Fe and O/S, indicates the progressive replacement of Fe–F coordination by Fe–(O/S) environments.

In the LPED electrolyte (Fig. 2c, d), EELS of the C K- and O K-edges show strong intensities only at the surface after the 1st cycle, while the related intensities increase in the intermediate region after the 125th cycle. In contrast, the Fe $L_{2,3}$- and F K-signals exhibit their lowest intensities at the surface but increase in the intermediate region after the 125th cycle. These results indicate that C/O-rich species initially confined to the interface gradually infiltrate deeper into the particles and interact with Fe during prolonged cycling. Given that EELS and EDX provide only elemental information, these results suggest the development of Fe environments associated with O, S, and C species.

The above phenomena indicate that the CEI on the positive electrode interface not only remains on the surface but also gradually penetrates into the interior of the particles as cycling proceeds. This is caused by the continuous pulverization of the particles during the conversion reaction and their sustained contact with the electrolyte. As a result, after multiple cycles, the FeF_3 particles evolve into compositionally heterogeneous and short-range ordered domains permeated by CEI-derived species, exhibiting electrolyte-dependent Fe–(O/S/C) coordination characteristics. Such element-specific overlaps between Fe and heteroatoms (O, S, and C) imply that distinct local bonding environments may emerge within the particles, potentially altering the intrinsic redox chemistry of FeF_3.

Multi-probe spectroscopy identifies amorphous motifs

To understand the elemental composition and valence state distribution of the positive electrode material after cycling, X-ray photoelectron spectroscopy (XPS) measurements were conducted at different stages (after 3 activation cycles at 0.1 C, with the initial state defined as the fully charged state of the 1st cycle): the 1st cycle of fully charging (1st FC), the 1st cycle of fully discharging (1st FD), the 125th cycle of fully charging (125th FC), and the 125th cycle of fully discharging (125th FD). Ion beam sputtering was performed prior to XPS measurement to enable in-depth analysis of elemental composition and phase structure by removing the interface layer. The XPS spectra of positive electrodes after 10 min of sputtering are shown in Fig. 3. First, the XPS results of the positive electrodes cycled in the LFDM electrolyte were analyzed to clarify the evolution of Fe, S, and O species during cycling.

The Fe 2*p* spectra in Fig. 3a reveal clear Fe^{2+} and Fe^{3+} peaks after the 1st FC and a distinct Fe^0 peak after the 1st FD, consistent with the theoretical conversion reaction process[20]. The partial persistence of Fe^{2+} in the charged state suggests that the oxidation of Fe is incomplete, likely due to limited Li^+ diffusion and reaction kinetics[21–23]. In the 125th FC and FD, both Fe^{2+} and Fe^{3+} peaks are clearly visible with similar intensities, indicating that the valence distribution of Fe becomes stabilized after long-term cycling, although a minor Fe^0 component is still detectable.

The S 2*p* spectra in Fig. 3b show that peaks above 166 eV mainly correspond to by-products of lithium salt decomposition (SO_x and SO_2F), while peaks below 166 eV are primarily elemental sulfur and lower-valence sulfur compounds, including S^- and S^{2-}. After the 1st FC, a large amount of low-valence sulfur, mainly in the form of Li_2S_2 at 163.6 eV with smaller amounts of Li_2S, is present, indicating the formation of CEI due to electrolyte decomposition during initial cycles. After the 1st FD, the intensity of the Li_2S peak at around 162.4 eV increases, indicating that lithium storage on the positive electrode side promotes the conversion of Li_2S_2 to Li_2S during discharge. After the 125th FC and FD, the sulfur peaks follow a similar trend to those after the first cycle, but with an enhanced low-binding-energy component (~161.8 eV), suggesting stronger Fe–S interaction after prolonged cycling. While direct identification of FeS species is not possible from XPS alone, the simultaneous presence of Fe^{2+} and S^{2-} indicates the formation of Fe–S coordination environments within the positive electrode.

The O 1*s* spectra (Fig. 3c) reveal distinct peaks corresponding to S = O, C = O, Li–O, and Fe–O bonds, arranged from high to low binding energies. After the 1 st FC and FD, the presence of S = O, C = O, and Li–O bonds are mainly attributed to the formation of the CEI. Following the 125th FC and FD, a weak but discernible Fe–O component emerges, indicating the appearance of localized Fe–O coordination. Additionally, the F 1*s* and C 1*s* spectra show little variation, as shown in Supplementary Fig. 16a, b, with the main peaks corresponding to Fe/Li–F (about 685 eV) and C–C (about 284.8 eV) bonds.

Fe 2*p* spectra of the positive electrodes after cycling in the LPED electrolyte (Fig. 3d) exhibit features consistent with those observed for the positive electrode cycled in the LFDM electrolyte after the initial charge–discharge cycle. A distinct Fe^{2+} peak is detected in the charged state after the first cycle, and a clear Fe^0 peak is present in the discharged state. After 125 cycles, Fe^{2+} and Fe^0 remain dominant, suggesting partial reduction and accumulation of electrochemically inactive Fe species. C 1*s* and O 1*s* spectra (Fig. 3e, f) reveal pronounced CO_3^{2-} peaks in the samples after 125 cycles, with the C 1*s* peak located around 289.5 eV and the O 1*s* peak around 532.1 eV. After 500 cycles, the C 1*s* spectrum of the positive electrode shows a more pronounced CO_3^{2-} peak, as shown in Supplementary Fig. 16c. In contrast, these carbonate-related features are nearly absent in the early cycles, confirming their gradual accumulation over time. Besides, the F 1*s* spectra of cycled FeF_3 positive electrode (Supplementary Fig. 16d) exhibit a Fe/Li–F peak around 685 eV. These findings suggest that carbonate species formed during long-term cycling may coordinate with Fe, giving rise to Fe–CO_3-like environments within the bulk.

To further understand the nature and distribution of carbonate species, depth-resolved XPS analysis was performed on the FeF_3@rGO electrode after the 125th cycle, with sputtering depths of 0 nm, 60 nm, and 180 nm. In the O 1*s* spectra (Fig. 3g), the carbonate-related peak gradually shifts toward higher binding energy with increasing depth. According to literature[34,35], the main O 1*s* peak of $FeCO_3$ typically

https://doi.org/10.1038/s41467-026-72471-z

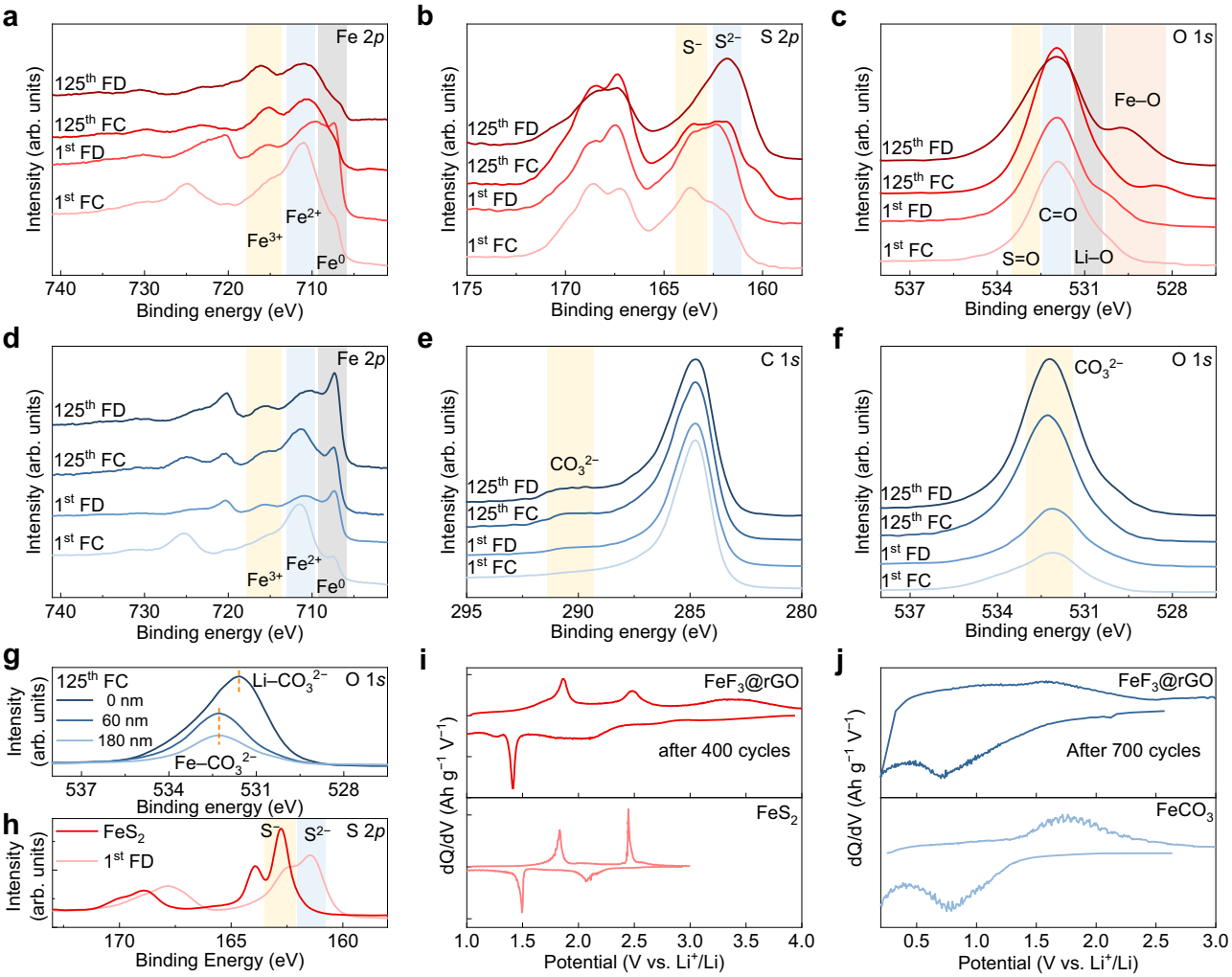

Fig. 3 | XPS analysis of electrolyte-dependent chemical species in cycled electrodes. XPS spectra of Fe 2*p* (**a**), S 2*p* (**b**) and O 1*s* (**c**) for cycled electrodes in LFDM electrolyte. XPS spectra of Fe 2*p* (**d**), C 1*s* (**e**) and O 1*s* (**f**) for cycled electrodes in LPED electrolyte. **g** Depth-resolved XPS spectra of O 1*s* for the 125th cycled FeF_3@rGO electrodes in LPED electrolyte. **h** XPS spectra of S 2*p* for pristine and first-discharged FeS_2 electrode. **i** Comparison of dQ/dV curves between cycled FeF_3@rGO (1.0–4.0 V) and FeS_2 (1.0–3.0 V) electrodes in LFDM electrolyte. **j** dQ/dV curves comparison between cycled FeF_3@rGO and $FeCO_3$ (0.2 V–3.0 V) electrodes in LPED electrolyte. Electrodes were harvested after cycling at 0.5 C (1 C = 712 mAh g^{-1}) and 25 ± 1 °C.

appears ~0.5 eV higher than that of Li_2CO_3, consistent with the observed difference between surface and bulk signals. A similar depth-dependent shift is also observed in the C 1*s* spectra (Supplementary Fig. 17a), while Fe 2*p* spectra (Supplementary Fig. 17b) show an increase in Fe^{2+} intensity with sputtering depth, suggesting the presence of Fe^{2+}-containing environments in deeper regions. In contrast, such depth-related features are absent in the 1 st-cycled electrode (Supplementary Fig. 17c–e), where Fe is primarily present as FeF_x, and no significant carbonate signals are detected in the O 1*s* or C 1*s* spectra. These results indicate that carbonate species are not limited to the CEI but extend into the particle interior, forming Fe–CO_3 coordination within the bulk.

To verify this interpretation, reference experiments were conducted using commercial FeS_2 and $FeCO_3$ electrodes. For FeS_2 in LFDM, the S 2*p* spectra (Fig. 3h) display a distinct S^- peak at 162.8 eV. After discharge, the electrode exhibits a stronger S^{2-} peak at 161.5 eV, indicating that sulfur undergoes a conversion process. Additionally, Fe 2*p* spectra (Supplementary Fig. 18) reveal that Fe does not transition to a lower oxidation state at this stage, suggesting that iron remains largely inactive, a behavior consistent with the long-cycled FeF_3 positive electrode in LFDM electrolyte.

The dQ/dV curves of FeF_3@rGO after 400 cycles and FeS_2 in the LFDM electrolyte show that the redox peaks of the cycled FeF_3 in the 1.0–3.0 V range correspond closely to the two redox pairs of FeS_2 (Fig. 3i), suggesting the development of Fe–S redox chemistry in the FeF_3 positive electrode after prolonged cycling. Similarly, the dQ/dV curves of FeF_3@rGO after 700 cycles and those of $FeCO_3$ in the LPED electrolyte are shown in Fig. 3j. Within the 0.2–3.0 V voltage range, the $FeCO_3$ electrode shows distinct redox peaks (oxidation at 1.75 V, reduction at 0.75 V), while the FeF_3 positive electrode after extended cycling exhibits weak peaks at similar positions, accompanied by a broad low-voltage region. This behavior is attributed to capacitive-like charge storage associated with residual Fe^0 nanoparticles and Fe–CO_3 interactions. Together, these results support that the long-term electrochemical behavior of FeF_3 evolves toward FeS_2-type chemistry in LFDM and $FeCO_3$-type chemistry in LPED, demonstrating the electrolyte-governed transformation of conversion pathways.

To further investigate the phase evolution of the material during cycling, synchrotron XRD (SXRD) technologies were used for phase change analysis on fresh and cycled FeF_3@rGO positive electrodes with sufficient mass loading (Fig. 4a). Aside from a background peak, no other distinct diffraction peaks were found after 125 cycles, suggesting that the active material had transformed from a crystalline to a disordered and amorphous state (rather smaller nanoparticles) during the cycling process. Then X-ray absorption spectroscopy (XAS) was

https://doi.org/10.1038/s41467-026-72471-z

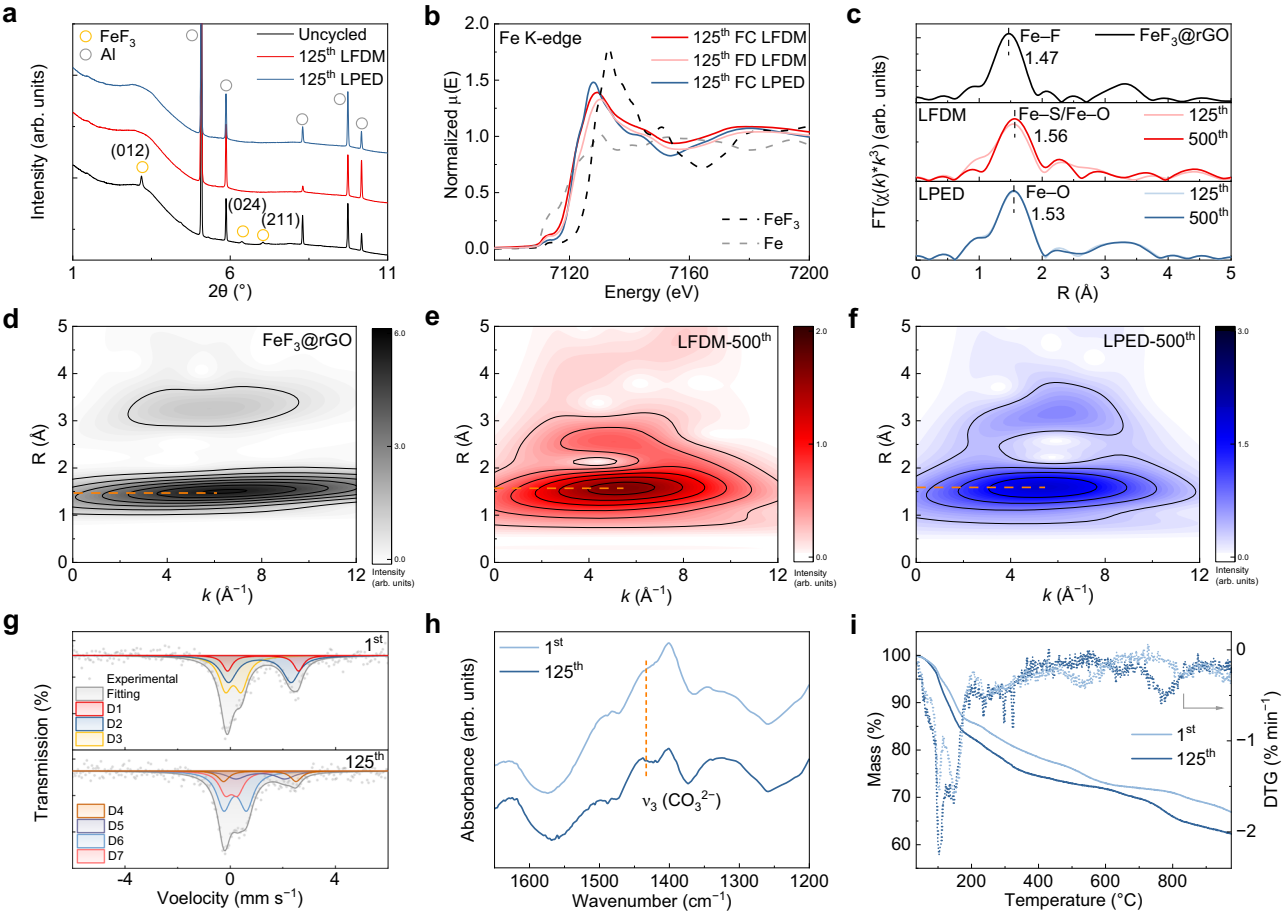

Fig. 4 | Structural evolution of FeF_3 electrodes in different electrolytes. a SXRD patterns of uncycled, 125th-cycled LFDM, and 125th-cycled LPED electrodes. **b** Normalized Fe K-edge XANES spectra of Fe foil, uncycled electrode, and 125th-cycled LFDM and LPED electrodes. XANES spectra were normalized using a standard pre-edge subtraction and post-edge normalization procedure. **c** Fourier transforms (k^3-weighted) of the Fe K-edge EXAFS spectra of uncycled, 125th, 500th-cycled LFDM and 125th, 500th-cycled LPED electrodes; Wavelet transforms of Fe K-edge EXAFS spectra for uncycled (**d**), 500th-cycled LFDM (**e**) and 500th-cycled LPED (**f**) electrodes. **g** ^{57}Fe Mössbauer spectra of first-cycled and 125th-cycled LFDM electrodes. FTIR spectra (**h**) and thermogravimetric analysis (**i**) of the electrodes after the first and 125th cycles. Cells were cycled between 1.0 and 4.0 V at 0.5 C (1 C = 712 mAh g^{-1}) and 25 ± 1 °C before disassembly.

performed to further examine the evolution of Fe valence states and local coordination environments before and after cycling. The Fe K-edge X-ray absorption near-edge structure (XANES) spectra of the 125th-cycled LFDM and LPED positive electrodes show noticeable edge shifts to 7120.7 eV and 7121.1 eV, respectively, compared with pristine FeF_3 (7127.7 eV) and Fe foil (7110.7 eV) (Fig. 4b)[24,25,36]. This edge shift is consistent with a reduction of Fe^{3+} toward lower-valence Fe species upon electrochemical cycling, indicating substantial changes in the Fe electronic structure. To further assess these electronic-state changes, linear combination fitting (LCF) of the XANES spectra was conducted using Fe-based reference compounds (Supplementary Fig. 19). Given the highly disordered and multiphase nature of the cycled electrodes, the XANES-LCF analysis is employed here to provide qualitative insight into Fe speciation trends, rather than to uniquely identify specific crystalline phases. Within this framework, the LFDM sample is well described by a combination of sulfide-like and oxide-like Fe reference components (Supplementary Fig. 20a and Supplementary Table 1), while the LPED sample exhibits a dominant contribution from carbonate- species together with metallic Fe references (Supplementary Fig. 20b and Supplementary Table 2), yielding R-factors below 3%. These results are consistent with the observed edge-position shifts and indicate pronounced electrolyte-dependent differences in the overall Fe chemical environment, rather than definitive phase formation, in the two systems. Additionally, a reduction of Fe^{3+} to metallic Fe^0 occurs during the first charge–discharge cycle in the LFDM electrolyte is suggested by the combined XANES and extended X-ray absorption fine structure (EXAFS) results (Supplementary Fig. 21a, b). However, after 125 cycles both charged and discharged electrodes display nearly identical edge positions (~7120.8 eV), indicating that Fe predominantly resides in a similar average oxidation state under steady-state cycling conditions, in agreement with the XPS analysis.

EXAFS analysis provides further insight into the coordination environment. The uncycled positive electrode, fitted using the FeF_3 model (Supplementary Fig. 21c–d and Supplementary Table 3), exhibits characteristic Fe–F shell at 1.47 Å. After prolonged cycling, the first-shell peak shifts toward longer distances (≈1.53–1.56 Å) in both electrolytes, implying a change in Fe bonding environment. In the LFDM electrolyte, the first shell can be associated with Fe–S or Fe–O coordination, whereas in LPED, it corresponds to Fe–O bonds typical of carbonate-type compounds. First-shell fitting results further support these assignments. For the LFDM sample, the fit was obtained by modeling two Fe-centered subshells at 2.18 Å (Fe–S) and 2.09 Å (Fe–O), with an approximate ratio of 56%:44%, consistent with mixed Fe–S/O coordination (Supplementary Fig. 20c and Supplementary Table 4). In addition, the LPED sample was well fitted by a single Fe–O path at 2.05 Å, consistent with carbonate-containing Fe–O local coordination environments (Supplementary Fig. 20d and Supplementary Table 5). The corresponding R-factors (1.3% and 0.3%, respectively) confirm good internal consistency of the fitting results and are consistent with the presence of distinct local Fe coordination environments in the two

systems. Meanwhile, a weak second-shell feature around 2.2 Å can still be discerned, which is likely associated with residual Fe–Fe coordination originating from metallic Fe^0 domains (Supplementary Fig. 21e). The consistency of XANES/EXAFS features between the 125th and 500th cycles suggests that structural reconstruction stabilizes after extensive cycling (Supplementary Fig. 21f). Wavelet transform (WT) EXAFS maps (Fig. 4d–f) further corroborate these findings, showing an intensity shift of the first-shell feature toward lower *k* and *R* regions, in line with the formation of heavier ligand coordination.

To cross-validate these interpretations, Mössbauer spectroscopy was employed for the LFDM-cycled electrodes (Fig. 4g and Supplementary Table 6). The 1st-cycle spectrum displays three doublets (D_1–D_3) with quadrupole splitting (QS) of 2.70, 2.38, and 0.60 mm s^{-1}, corresponding to Li_xFeF_3, FeF_2, and FeF_3, respectively[37–39]. After 125 cycles, four additional doublets (D_4–D_7; QS = 2.76, 1.87, 0.86, 0.47 mm s^{-1}) emerge, indicating multiple Fe environments consistent with Fe–S and Fe–O bonding motifs (e.g., FeS_2, Fe_3O_4-like, and FeO-like species)[40–43]. These observations align well with the XPS-derived coordination evolution.

Complementary Fourier transform infrared (FTIR) spectra and thermogravimetric analysis (TGA) were conducted for LPED-cycled electrodes to confirm carbonate formation. After 125 cycles, FTIR spectra display characteristic ν_3 (~1400 cm^{-1}) and ν_2 (~800 cm^{-1}) bands of CO_3^{2-} with broadened, red-shifted profiles, typical of Fe^{2+}–CO_3 coordination (Fig. 4h and Supplementary Fig. 22). An Fe–O vibrational feature (~425 cm^{-1}) further supports this assignment. In contrast, the 1st-cycled sample exhibits sharper bands near 1470 and 865 cm^{-1}, consistent with Li_2CO_3. TGA results (Fig. 4i) reveal a distinct weight-loss event between 200 and 350 °C in the long-cycled electrode, absent in the 1st-cycled one, corresponding to the decomposition range of $FeCO_3$. These complementary results corroborate that FeF_3 evolves toward FeS_y/FeO_z- and $FeCO_3$-type species in LFDM and LPED electrolytes, respectively, establishing direct spectroscopic evidence for electrolyte-dependent anion-driven conversion pathways.

Interfacial anion competition dictates the fate of FeF_3 electrodes

The evolution of anions in the CEI plays a critical role in the reaction process[44]. Studies indicate that transition metals have a catalytic effect on the electrolyte, thereby promoting the formation of diverse CEI components[45–47]. When the FeF_3 positive electrode is in a discharged state, a large number of nano-sized iron particles are produced. Some of these iron particles are directly exposed to the electrolyte, making them prone to interactions with the electrolyte. Such catalytic interactions between Fe nanoparticles and electrolyte species were experimentally confirmed in both electrolytes (Supplementary Fig. 23), revealing Fe's ability to accelerate CEI formation. To gain a deeper understanding of this catalytic behavior, density functional theory (DFT) calculations were performed to evaluate the binding strength and decomposition tendency of various electrolyte components on Fe(110) surfaces.

Calculations reveal that the adsorption binding energy of Fe(110) varies among electrolyte components, indicating different affinities of iron for these species. All DFT total energies were computed without entropic or zero-point energy corrections, and represent relative stabilities of decomposition intermediates. Negative adsorption energies across all simulated systems indicate thermodynamically favorable interactions (Fig. 5a). In the LFDM electrolyte, the binding energies of Fe with DME (−0.68 eV) and LiFSI (−0.64 eV) are relatively close. For components in the LPED electrolyte, the lowest binding energy is with EC (−0.57 eV), followed by DMC (−0.49 eV) and LiPF6 (−0.27 eV). Although solvent-displacement effects were not explicitly included, the energetic trend remains consistent, showing stronger Fe–solvent interactions in the ether-based system.

Given the high concentration of LiFSI in the electrolyte, Fe–LiFSI interactions are statistically more likely to occur. Figure 5b shows the calculated Gibbs free energy for LiFSI decomposition with and without Fe catalysis, demonstrating that Fe substantially lowers the decomposition barrier. Under Fe catalysis, the S = O, S–F, and S–N bonds in LiFSI become more labile, making bond cleavage energetically favorable and leading to the generation of Li_2S and Li_2O, which adhere to the positive electrode interface to form the CEI. Similarly, Fe-catalyzed EC decomposition (Fig. 5c) decreases the reaction energies for CO_2 and CO_3^{2-} formation (−0.39 eV and −1.42 eV, respectively), favoring Li_2CO_3 generation within the CEI. These findings suggest that Fe nanoparticles act as catalytic centers that accelerate electrolyte decomposition and shape the interfacial composition during cycling. Such catalytic reactions also imply that during subsequent charging, Fe nanoparticles can further interact with pre-existing lithium salts within the CEI, promoting secondary reactions at the interface.

To further explore iron's interactions with various lithium salts, we calculated the standard electrode potentials of reactions between Fe and different lithium compounds based on their Gibbs free energy changes (Supplementary Note 3). As shown in Fig. 5d, the formation of FeF_3 and FeF_2 corresponds to higher electrode potentials of 2.75 V and 2.68 V (vs. Li^+/Li), indicating strong thermodynamic driving forces. In contrast, the formation of FeO, FeS, and $FeCO_3$ yields lower standard potentials of 1.61, 1.74, and 2.41 V, respectively, while Fe_2O_3 and FeS_2 exhibit intermediate values of 1.63 V and 1.86 V. These products correspond to naturally stable oxide, sulfide, and carbonate phases, reflecting their higher thermodynamic stability under O-, S-, or CO_3-rich conditions. This hierarchy suggests that Fe nanoparticles preferentially react with Li_2O, Li_2S, and Li_2CO_3 rather than LiF, following the reactivity order $Li_2O > Li_2S > Li_2CO_3 > LiF$ (Fig. 5e). Such a thermodynamic preference provides a rational explanation for the distinct phase-evolution pathways observed in the two electrolytes.

To better understand the kinetic limitations associated with the subsequent phase evolution, we further examined the intrinsic Fe^{2+} mobility within various Fe(II)-containing compounds. As summarized in Supplementary Fig. 24, DFT calculations reveal that the migration barriers for Fe^{2+} diffusion in FeF_2, FeO, FeS, and $FeCO_3$ are all relatively high (0.9–3.1 eV), indicating that bulk cation diffusion is energetically unfavorable at typical battery operating temperatures. Such large activation energies suggest that long-range Fe^{2+} diffusion through the crystalline lattice is kinetically hindered, and therefore unlikely to govern the overall transformation. Instead, the observed phase conversion and redistribution of Fe species are more plausibly facilitated by disordered regions, grain boundaries, and interfacial pathways, where structural flexibility and higher defect densities can substantially lower the effective diffusion barriers.

Building upon these thermodynamic results, Fig. 5f illustrates the proposed phase-evolution mechanism of FeF_3 in LFDM and LPED electrolytes. In the LFDM electrolyte, FeF_3 initially serves as the active positive electrode material. During cycling, nano-sized Fe particles catalyze the decomposition of solvent and salt molecules, generating Li_2S and Li_2O that subsequently react with Fe to form FeS- and FeO-type phases. After extended cycling, FeS_y and FeO_z become dominant, coexisting with a LiF-rich core and traces of Fe^0. Because FeS_y-type species remain electrochemically active within 1.0–4.0 V, this transformation accounts for the "negative fading" behavior and sustained reversible cycling observed in the LFDM electrolyte. In contrast, in the LPED electrolyte, EC decomposition predominantly yields Li_2CO_3, which reacts with Fe to form carbonate-rich species that are electrochemically inactive within this potential window. The deposition of $FeCO_3$ on particle surfaces blocks Li^+ transport and electron conduction, progressively isolating the active regions and causing Fe^0 accumulation during prolonged cycling.

While electrolyte decomposition during FeF_3 conversion is relatively limited, the interfacial reactions it induces have a profound influence on phase evolution and reversibility. This underscores the critical role of electrolyte design and interface regulation in mitigating

https://doi.org/10.1038/s41467-026-72471-z

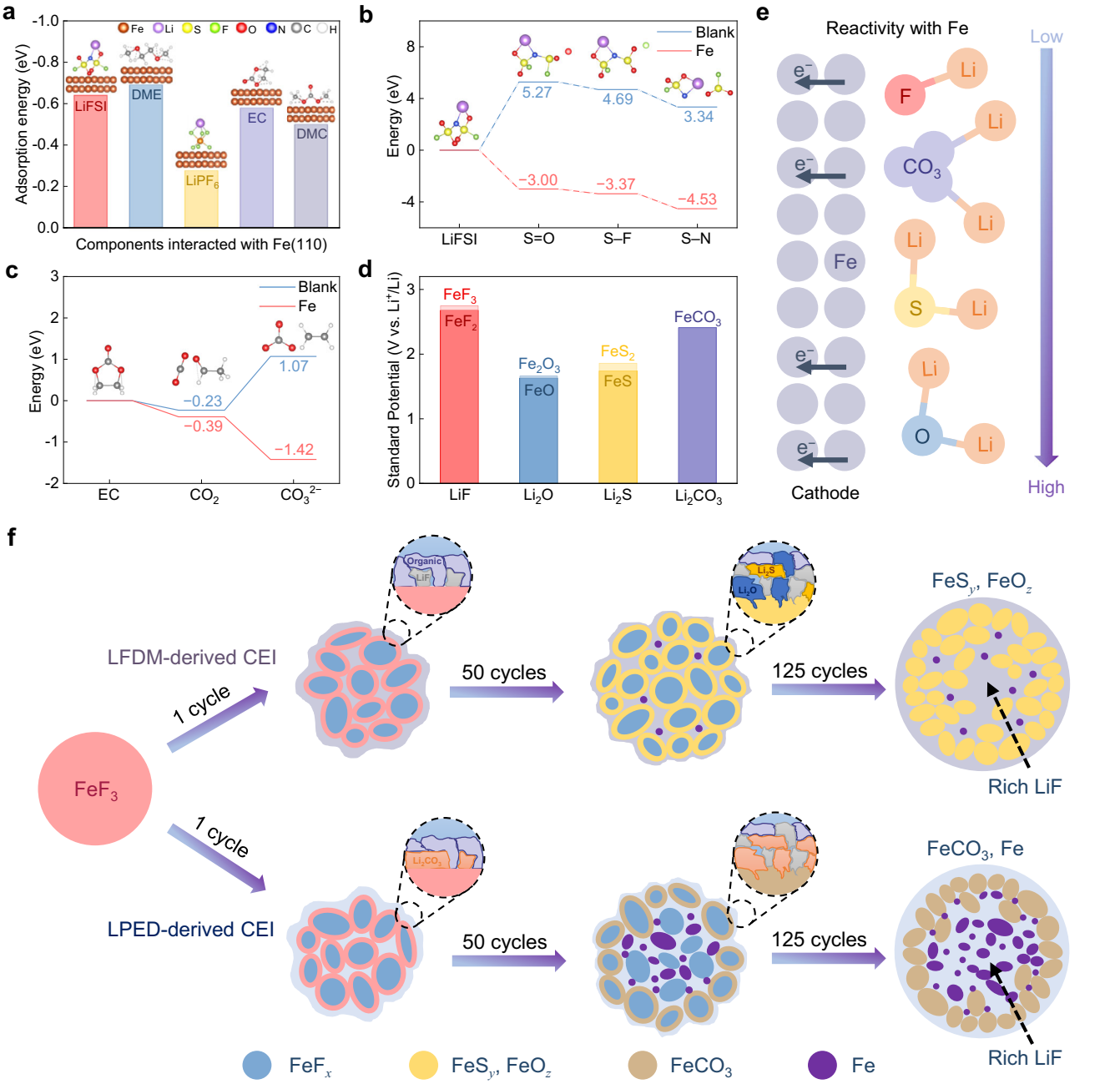

Fig. 5 | Electrolyte-dependent phase evolution of FeF_3 electrodes during cycling. a Binding energy of LiFSI, DME, $LiPF_6$, EC, and DMC on the Fe(110) surface. Energy profiles for bond breaking of LiFSI (**b**) and EC (**c**) on different paths. **d** Calculated standard electrode potentials (vs. Li^+/Li) of various lithium salts combining with iron, calculated from ΔG° values. **e** schematic illustration of the competing chemical reactions of different lithium compounds with iron; **f** schematic illustration of the electrolyte-dependent phase evolution during cycling.

parasitic processes and sustaining reversible electrochemical activity. Integrating thermodynamic and spectroscopic evidence, we propose a unified mechanism whereby interfacial anion chemistry dictates the structural and electrochemical evolution of FeF_3 positive electrodes.

Discussion

In summary, this work investigates a clear electrolyte-dependent divergence in the electrochemical behavior of FeF_3 positive electrodes. In conventional electrolytes, FeF_3 indeed behaves as a poor and unstable conversion electrode, exhibiting rapid degradation and loss of reversibility, whereas our work establishes a comprehensive mechanistic framework linking interfacial anion chemistry to phase evolution during cycling. Through the integration of detailed electrochemical analyses, advanced structural characterizations, and thermodynamic modeling, we investigate how electrolyte composition dictates the structural fate and reversibility of FeF_3. Because conventional XRD cannot resolve the amorphous phases formed after long-term cycling, we employed complementary spectroscopic and microscopic techniques to overcome this limitation and reveal the hidden structural evolution. The CEI composition is identified as a decisive factor controlling phase evolution. In the LFDM electrolyte, the CEI enriched with Li_2S and Li_2O readily interacts with Fe to form electrochemically active iron sulfides, which sustain reversible redox processes. In contrast, the LPED electrolyte predominantly generates Li_2CO_3, which reacts with Fe to form insulating and electrochemically inert $FeCO_3$ within the 1.0–4.0 V window, leading to rapid capacity

fading. The nanoscale Fe formed during discharge further catalyzes electrolyte decomposition, reinforcing this electrolyte-dependent divergence. These results reveal that interfacial anion competition governs Fe coordination and phase evolution during cycling. Given the intrinsically disordered nature of the final products, future pair distribution function or cryo-TEM studies could provide complementary insight into their short-range configurations. Crucially, the long-term behavior of FeF_3 positive electrodes is governed by whether the resulting Fe-based phases remain electrochemically active within the operating potential window. While sulfide species retain redox activity, oxides and carbonates do not, which explains the contrasting degradation pathways and electrochemical behaviors observed between ether- and ester-based systems. These findings highlight the role of interfacial anion chemistry in governing phase evolution and degradation pathways in FeF_3 conversion electrodes, and provide insights into related iron-based fluoride conversion systems.

Methods

Materials preparation

0.85 g of $Fe(NO_3)_3{\cdot}9H_2O$ (Macklin, China, >99.5%) was added to deionized water (15 mL) to form a solution, followed by the addition of 0.36 g urea (Aladdin, China, >99.5%) and 1.35 g polyvinylpyrrolidone K30 (Aladdin, China, >99%). Next, 58 mL of graphene oxide (GO) aqueous dispersion (2 g L^{-1}, Suzhou TANFENG graphene Tech Co., Ltd, China) and 0.288 g of carbon nanotube (CNT) aqueous dispersion (10 wt.%, SUSN, China) were added to the above solution with ultrasonication and stirring for 3 h. Later, the mixture sealed in a Teflon-lined stainless-steel autoclave and maintained at 200 °C for 8 h. After cooling down, the hydrogel was washed with deionized water three times by centrifugation. After adding 30 mL deionized water into the obtained deposits, the solution was frozen quickly using liquid nitrogen and freeze-dried at −60 °C under vacuum for 72 h. After that, the Fe_2O_3@rGO composite was obtained. The Fe_2O_3@rGO composite was placed in a tube furnace and calcined at 720 °C for 2 h under an argon atmosphere to obtain the Fe@rGO composite. It was then reacted at 280 °C for 2 h in a nitrogen trifluoride atmosphere, resulting in the final FeF_3@rGO composite. The weight ratio of FeF_3 in the FeF_3@rGO composite is approximately 70%, and the detailed calculation is provided in Supplementary Note 1.

Electrochemical characterization

The synthesized FeF_3@rGO composite was used as the active material and mixed with conductive carbon black (Super P, MTI Corp., USA, >99%) and polyvinylidene fluoride (PVDF, ARKEMA, France, >99%, M_w = 600,000) in a mass ratio of 80:10:10. The mixture was prepared in an argon-filled glovebox (H_2O and O_2 < 0.01 ppm; Mikrouna, China), with the addition of a suitable amount of N-methyl-2-pyrrolidone (NMP, DoDoChem, China, anhydrous), followed by thorough grinding and homogeneous mixing to form a slurry. Using a Doctor blade coater, the slurry was evenly coated onto aluminum foil (15 μm thick, Bikeman, China, >99.5%), which was subsequently heated at 80 °C for 12 h on a hot plate inside the glovebox to obtain the dried electrode sheet. Finally, the dried electrode was cut into 12 mm diameter circular positive electrodes using a punch machine. The mass loading of the active material (FeF_3 only) in the electrodes is approximately 1.5 −1.8 mg cm^{-2}, corresponding to an electrode coating thickness of ~20−30 μm (excluding the current collector).

Additional electrodes based on commercial powders were prepared using Fe (Aladdin, China, 99.9%), FeF_2 (Sigma-Aldrich, USA, 98%), FeF_3 (Alfa Aesar, USA, >97%), FeS_2 (Macklin, China, 99%), and $FeCO_3$ (Aladdin, China, 99%) as active materials. In these electrodes, the mass ratio of active material, conductive carbon, and binder was fixed at 70:20:10. All other procedures, including slurry preparation, coating, drying, and electrode punching, were identical to those described above.

A LiFSI-DME electrolyte was prepared by dissolving 1.741 g of LiFSI in 0.75 mL of DME solvent, yielding a lithium salt concentration of 4.6 M. A commercial electrolyte consisting of 1 M $LiPF_6$ in EC/DMC (1:1, v/v) was also used. The lithium salt, solvent, and commercial electrolyte were purchased from DoDoChem (China) with battery-grade purity (purity ≥99.9%, $H_2O \leq 20$ ppm) and used as received without further purification or drying. All electrochemical tests were performed under excess-electrolyte conditions to minimize kinetic limitations and focus on the intrinsic chemical differences between ether- and ester-based electrolytes.

Using the prepared electrodes as the working electrode, lithium metal foil (15.6 mm in diameter and 0.45 mm thick, China Energy Lithium Co., Ltd., China, >99.5%) as the counter/reference electrode, and a polypropylene/polyethylene microporous film (Celgard 2400, USA) as the separator, CR2025-type coin cells with SUS304 stainless-steel cases and stainless-steel springs (MTI Corporation, China) were assembled in the glovebox with 60 μL of electrolyte added to each cell. The cells were tested for charge/discharge cycling between 1.0 and 4.0 V using a LAND battery test system (Wuhan LANHE Instruments, China), with a specific current corresponding to 1 C = 712 mA g^{-1}. Coulombic efficiency (CE) was calculated as the ratio of charge capacity to discharge capacity during cycling. CV and EIS measurements were performed using a Gamry electrochemical workstation (Reference 600 + , Gamry Instruments, USA), where the CV voltage range was set to 1.0−4.0 V with a sweep rate of 0.3 mV s^{-1}. EIS measurements were conducted in potentiostatic mode with an AC perturbation amplitude of 10 mV over a frequency range from 0.1 Hz to 10^5 Hz. Both freshly assembled cells and cycled cells (at the fully charged state) were rested at open-circuit voltage for 6 h prior to EIS measurements to ensure quasi-equilibrium conditions. All electrochemical measurements were carried out in a temperature-controlled chamber at 25 ± 1 °C.

Materials characterization

The morphology of the samples was examined using SEM (MIRA3 LMH, TESCAN, Czech Republic). SEM images were obtained using an accelerating voltage of 20 kV.

This study utilized two types of XRD instruments: a conventional polycrystalline X-ray diffractometer (Empyrean, Malvern PANalytical, The Netherlands), and a SXRD system. The SXRD measurements were conducted using the PETRA III light source at the beamline P02.1 of the Deutsches Elektronen-Synchrotron (DESY) in Hamburg, Germany[48]. The conventional XRD patterns were collected using a Cu target with a wavelength (λ) of 1.54056 Å over a 2θ range of 10−80°, with a step size of 0.013° and a scanning rate of 5° min^{-1}. The SXRD used X-rays with λ of 0.207337 Å.

HRTEM images were acquired using a Tecnai F20 transmission electron microscope (FEI Company, USA) operated at 200 kV. For enhanced imaging and elemental analysis, HAADF-STEM was integrated with EELS, utilizing the Gatan Quantum energy filter (Gatan Inc., USA). Cycled positive electrodes for TEM analysis were prepared by soaking in NMP at 25 ± 2 °C for 5 days to remove PVDF. The exposure of sample to air during transfer to TEM was minimized to less than 30 s.

XPS measurements were performed using a Thermo Scientific Nexsa spectrometer (Thermo Fisher Scientific, USA). The spectra were collected using Al Kα radiation (1486.6 eV), and the binding energies were calibrated using the C 1 s peak at 284.8 eV.

The XAS experiments were conducted at the P65 beamline of the PETRA III synchrotron facility at the DESY, Germany. The spectra were collected at 25 ± 2 °C under air-free conditions by encapsulating the samples with Kapton film. For energy calibration, a metallic iron reference sample was placed in the beam path, and the position of the maximum of the first derivative of the XANES spectrum was defined as the K-edge E_0 value, which was calibrated to 7110.5 eV. XAS data were processed and analyzed using the Demeter software suite[49]. A linear function was first subtracted from the pre-edge region, and the

post-edge jump was normalized using the Athena software. To isolate the $\chi(k)$ data, a smooth polynomial was subtracted to approximate the atomic absorption background. After applying a window function ($\Delta k = 10$ Å^{-1}), a k^3-weighted Fourier transform of the $\chi(k)$ data was performed. Structural parameters were obtained by non-linear least-squares fitting of the EXAFS data in *R*-space using Artemis software. Additionally, wavelet transform analysis was performed using the HAMA Fortran software for better visualization[50,51], enabling further distinction between coordinating atoms with similar *R*-space positions but significantly different atomic numbers.

The Mössbauer spectra for this test were recorded using a Wissel MR-2500 Mössbauer spectrometer with a ^{57}Co/*Rh* radioactive source in transmission geometry at 25 ± 2 °C without an external magnetic field. The collected data were fitted and analyzed using MossWinn 4.0 software, and the velocity scale was calibrated using α-Fe foil.

TGA was performed using a STA2500 thermal analyzer (NETZSCH, Germany) under an argon atmosphere. The samples were heated from 25 to 1000 °C at a heating rate of 10 °C min^{-1} with an Ar flow rate of 20 mL min^{-1}.

FTIR spectra were recorded using a Nicolet iS50 spectrometer (Thermo Fisher Scientific, USA) equipped with a DTGS KBr detector. The spectra were collected in the range of 400–4000 cm^{-1} with a spectral resolution of 4 cm^{-1}, and 32 scans were accumulated for each spectrum.

After cycling, the cells were disassembled in an Ar-filled glovebox. The electrodes were washed with DME to remove residual electrolyte and subsequently dried under vacuum before characterization. All cycled sample preparation procedures were carried out under an Ar atmosphere at 25 ± 2 °C. SEM, XPS, and Mössbauer spectroscopy measurements were performed using vacuum-transfer holders to prevent air exposure. For XAS and SXRD measurements, the electrodes were sealed with Kapton tape in an Ar-filled glovebox before testing. For TEM, TGA, and FTIR measurements, the samples were prepared in an Ar-filled glovebox and transferred to the instruments under Ar protection. The samples were rapidly loaded into the instruments, with the air exposure time limited to less than 30 s to minimize possible influence. Unless otherwise specified, all measurements were performed at 25 ± 2 °C.

Calculations

All spin-polarized density functional theory (DFT) calculations were performed using the generalized gradient approximation (GGA) with the Perdew-Burke-Ernzerhof (PBE) functional to describe electron exchange–correlation effects, as implemented in the Vienna ab initio simulation package and the CASTEP code for cross-validation. The projector-augmented wave (PAW) method was adopted to represent the ionic cores. A plane-wave cutoff energy of 500–550 eV was used in all calculations, and Grimme's DFT-D3 dispersion correction was applied to account for van der Waals (vdW) interactions. For thermodynamic analysis, binding energies and energies of electrolyte component interactions with metallic Fe were calculated to assess reaction preferences. For kinetic analysis, the migration barriers of Fe^{2+} ions in representative Fe^{2+}-containing compounds (FeF_2, FeO, FeS and $FeCO_3$) were evaluated using the nudged elastic band (NEB) method. The Brillouin zone was sampled with Monkhorst–Pack k-point grids (e.g., 6 × 6 × 6) for structural relaxation and electronic structure calculations. The detailed DFT-optimized unit cell parameters for these materials are summarized in Supplementary Table 7. To better capture the localized electronic states of Fe 3d orbitals in mixed-valence systems, an onsite Coulomb correction (U–J = 5 eV) was applied. The convergence thresholds were set to a self-consistent field (SCF) energy tolerance of 1.0×10^{-5} eV/atom, a maximum force of 0.03 eV/Å, a maximum stress of 0.05 GPa, and a maximum displacement of 0.001 Å. All Fe salts were modeled in the ferromagnetic state, as the energy difference with antiferromagnetic configurations was negligible. The optimized atomic coordinates used for the DFT calculations are provided in Supplementary Data 1.

Data availability

Source data are provided with this paper. The source data have been deposited in Figshare and are publicly available at https://doi.org/10.6084/m9.figshare.28749764.

References

1. Cai, W. et al. A review on energy chemistry of fast-charging anodes. *Chem. Soc. Rev.* **49**, 3806–3833 (2020).
2. Viswanathan, V. et al. The challenges and opportunities of battery-powered flight. *Nature* **601**, 519–525 (2022).
3. Wu, F., Maier, J. & Yu, Y. Guidelines and trends for next-generation rechargeable lithium and lithium-ion batteries. *Chem. Soc. Rev.* **49**, 1569–1614 (2020).
4. Wu, F. & Yushin, G. Conversion cathodes for rechargeable lithium and lithium-ion batteries. *Energy Environ. Sci.* **10**, 435–459 (2017).
5. Wang, L. et al. Li-free cathode materials for high energy density lithium batteries. *Joule* **3**, 2086–2102 (2019).
6. Turcheniuk, K., Bondarev, D., Amatucci, G. G. & Yushin, G. Battery materials for low-cost electric transportation. *Mater. Today* **42**, 57–72 (2021).
7. Zhao, E. et al. Lithium–iron (III) fluoride battery with double surface protection. *Adv. Energy Mater.* **8**, 1800721 (2018).
8. Wu, F. et al. 3D honeycomb architecture enables a high-rate and long-life iron (III) fluoride-lithium battery. *Adv. Mater.* **31**, 1905146 (2019).
9. Wang, Y. et al. Prussian blue microcubes-derived FeF_3 cathodes for high-energy and ultra-stable lithium and lithium-ion batteries. *J. Power Sour.* **577**, 233234 (2023).
10. Zhou, X. et al. Cryo-TEM study of high-performance iron difluoride cathode enabled by low temperature CVD carbon coating. *Adv. Funct. Mater.* **34**, 2307131 (2023).
11. Wang, Y. et al. High-performance honeycombed FeF_3@C cathodes enabling practical lithium pouch cells and silicon–metal fluoride batteries. *Energy Storage Mater.* **60**, 102847 (2023).
12. Jiang, Z. et al. Multicore–shell iron fluoride@carbon microspheres as a long-life cathode for high-energy lithium batteries. *J. Mater. Chem. A* **11**, 21541–21552 (2023).
13. Liu, Y. et al. Reversible iron oxyfluoride (FeOF)-graphene composites as sustainable cathodes for high energy density lithium batteries. *Small* **19**, 2206947 (2023).
14. Huang, Q. et al. Insights into the effects of electrolyte composition on the performance and stability of FeF_2 conversion-type cathodes. *Adv. Energy Mater.* **9**, 1803323 (2019).
15. Wygant, B. R. et al. The role of electrolyte composition in enabling Li metal-iron fluoride full-cell batteries. *Adv. Sci.* **9**, 2105803 (2022).
16. Gu, W. et al. Lithium-iron fluoride battery with in situ surface protection. *Adv. Funct. Mater.* **26**, 1507–1516 (2016).
17. Fu, W. et al. Iron fluoride–carbon nanocomposite nanofibers as free-standing cathodes for high-energy lithium batteries. *Adv. Funct. Mater.* **28**, 1801711 (2018).
18. Xiao, A. W. et al. Understanding the conversion mechanism and performance of monodisperse FeF_2 nanocrystal cathodes. *Nat. Mater.* **19**, 644–654 (2020).
19. Senoh, H. et al. Degradation mechanism of conversion-type iron trifluoride: toward improvement of cycle performance. *ACS Appl. Mater. Interfaces* **11**, 30959–30967 (2019).
20. Liu, S. et al. Exploiting the iron difluoride electrochemistry by constructing hierarchical electron pathways and cathode electrolyte interface. *Small* **18**, 2202006 (2022).
21. Olbrich, L. F. et al. Iron fluoride-lithium metal batteries in bis(-fluorosulfonyl)imide-based ionic liquid electrolytes. *Cell Rep. Phys. Sci.* **5**, 101787 (2024).

22. Hua, X. et al. Revisiting metal fluorides as lithium-ion battery cathodes. *Nat. Mater.* **20**, 841–850 (2021).
23. Karki, K. et al. Revisiting conversion reaction mechanisms in lithium batteries: lithiation-driven topotactic transformation in FeF_2. *J. Am. Chem. Soc.* **140**, 17915–17922 (2018).
24. Li, L. et al. Origins of large voltage hysteresis in high-energy-density metal fluoride lithium-ion battery conversion electrodes. *J. Am. Chem. Soc.* **138**, 2838–2848 (2016).
25. Li, L. et al. Visualization of electrochemically driven solid-state phase transformations using operando hard X-ray spectro-imaging. *Nat. Commun.* **6**, 6883 (2015).
26. Wang, F. et al. Tracking lithium transport and electrochemical reactions in nanoparticles. *Nat. Commun.* **3**, 1201 (2012).
27. Wang, F. et al. Conversion reaction mechanisms in lithium ion batteries: study of the binary metal fluoride electrodes. *J. Am. Chem. Soc.* **133**, 18828–18836 (2011).
28. Kim, H. et al. Exploring anomalous charge storage in anode materials for next-generation Li rechargeable batteries. *Chem. Rev.* **120**, 6934–6976 (2020).
29. Wan, T. H. et al. Influence of the discretization methods on the distribution of relaxation times deconvolution: implementing radial basis functions with DRTtools. *Electrochim. Acta* **184**, 483–499 (2015).
30. Fang, Q. et al. Interfacial degradation of silicon anodes in pouch cells. *Energy Environ. Sci.* **17**, 6368–6376 (2024).
31. Cosandey, F., Al-Sharab, J. F., Badway, F., Amatucci, G. G. & Stadelmann, P. EELS spectroscopy of iron fluorides and FeF_x/C nanocomposite electrodes used in Li-ion batteries. *Microsc. Microanal.* **13**, 87–95 (2007).
32. Yu, M. et al. Unlocking iron metal as a cathode for sustainable Li-ion batteries by an anion solid solution. *Sci. Adv.* **10**, 4441 (2024).
33. Chen, X. et al. Bottom-up assembly of yolk-shell FeF_3@C nanocomposites as high-rate, long-term and air-stable cathodes. *Mater. Today* **81**, 47–58 (2024).
34. Zhang, C. et al. One step hydrothermal synthesis of $FeCO_3$ cubes for high performance lithium-ion battery anodes. *Electrochim. Acta* **182**, 559–564 (2015).
35. Yang, M. et al. Li_2CO_3/LiF-rich solid electrolyte interface stabilized lithium metal anodes for durable Li–CO_2 batteries. *Energy Storage Mater.* **73**, 103843 (2024).
36. Mori, M. et al. First-principles calculations of the atomic structure and electronic states of Li_xFeF_3. *Phys. Rev. B* **100**, 035128 (2019).
37. Singh, R. et al. Reversible control of magnetism: on the conversion of hydrated FeF_3 with Li to Fe and LiF. *J. Mater. Chem. A* **7**, 24005–24011 (2019).
38. Pohl, A. et al. Development of a water based process for stable conversion cathodes on the basis of FeF_3. *J. Power Sour.* **313**, 213–222 (2016).
39. Conte, D. E. et al. Operando Mössbauer spectroscopy investigation of the electrochemical reaction with lithium in bronze-type $FeF_3{\cdot}0.33H_2O$. *J. Phys. Chem. C.* **120**, 23933–23943 (2016).
40. Chin, P. P., Ding, J., Yi, J. B. & Liu, B. H. Synthesis of FeS_2 and FeS nanoparticles by high-energy mechanical milling and mechanochemical processing. *J. Alloy. Compd.* **390**, 255–260 (2005).
41. Yokoyama, D., Namiki, K. & Yamada, Y. Mössbauer study of Fe/S and Fe/O films produced by laser ablation of pyrite and hematite. *J. Radioanal. Nucl. Chem.* **268**, 283–288 (2006).
42. Komaba, S. et al. Electrochemical insertion of Li and Na ions into nanocrystalline Fe_3O_4 and α-Fe_2O_3 for rechargeable batteries. *J. Electrochem. Soc.* **157**, A60–A65 (2010).
43. Ati, M. et al. Single-step synthesis of $FeSO_4F_{1-y}OH_y$ ($0 \le y \le 1$) positive electrodes for Li-based batteries. *Chem. Mater.* **24**, 1472–1485 (2012).
44. Yu, W. et al. Electrochemical formation of bis(fluorosulfonyl)imide-derived solid-electrolyte interphase at Li-metal potential. *Nat. Chem.* **17**, 246–255 (2025).
45. Wang, C. et al. Overlooked electrolyte destabilization by manganese (II) in lithium-ion batteries. *Nat. Commun.* **10**, 3423 (2019).
46. Zhan, C., Wu, T., Lu, J. & Amine, K. Dissolution, migration, and deposition of transition metal ions in Li-ion batteries exemplified by Mn-based cathodes - a critical review. *Energy Environ. Sci.* **11**, 243–257 (2018).
47. Solchenbach, S., Hong, G., Freiberg, A. T. S., Jung, R. & Gasteiger, H. A. Electrolyte and SEI decomposition reactions of transition metal ions investigated by on-line electrochemical mass spectrometry. *J. Electrochem. Soc.* **165**, A3304–A3312 (2018).
48. Dippel, A. C. et al. Beamline P02.1 at PETRA III for high-resolution and high-energy powder diffraction. *J. Synchrotron Radiat.* **22**, 675–687 (2015).
49. Ravel, B. & Newville, M. ATHENA, ARTEMIS, HEPHAESTUS: data analysis for X-ray absorption spectroscopy using IFEFFIT. *J. Synchrotron Radiat.* **12**, 537–541 (2005).
50. Funke, H., Scheinost, A. C. & Chukalina, M. Wavelet analysis of extended x-ray absorption fine structure data. *Phys. Rev. B* **71**, 094110 (2005).
51. Funke, H., Chukalina, M. & Scheinost, A. C. A new FEFF-based wavelet for EXAFS data analysis. *J. Synchrotron Radiat.* **14**, 426–432 (2007).

Acknowledgements

The authors gratefully acknowledge financial support from the National Natural Science Foundation of China (No. 22479162 to F.W.), the Hunan Provincial Natural Science Foundation Project (No. 2025JJ30019 to F.W.), the Scientific Research Project of the Education Department of Hunan Province (No. 24A0017 to F.W.) and the Science and Technology Innovation Program of Hunan Province (No. 2023RC1016 to F.W.). P.F. also acknowledges the Fundação para a Ciência e a Tecnologia (FCT) for its financial support via the project LAETA Base Funding (DOI: 10.54499/UIDB/50022/2020).

Author contributions

Z.J., S.L. and F.W. conceived the idea for the project. Z.J., S.L. and P.W. prepared the materials and carried out electrochemical experiments. J.P. performed SRXRD and XAS measurements. Z.J., P.W. and F.C. performed the SEM, XRD, XPS, TGA, FTIR, and Mössbauer spectroscopy analyses. S.L. and P.F. acquired and analyzed the TEM data. Z.J., M.H., F.C. and J.L. conducted the simulations and analyzed the data. Z.J., S.L. and F.W. wrote the manuscript with input from all the coauthors.

Competing interests

The authors declare no competing interests.

Additional information

Supplementary information The online version contains supplementary material available at https://doi.org/10.1038/s41467-026-72471-z.

Correspondence and requests for materials should be addressed to Feixiang Wu.

Peer review information *Nature Communications* thanks Feng Wang, Katia Guérin and the other, anonymous, reviewer(s) for their contribution to the peer review of this work. A peer review file is available.